The Thesis Committee for Xuejing Jiao
Certifies that this is the approved version of the following thesis:

Pulsed photoneutron source driven by electrons from laser wakefield acceleration

APPROVED BY
SUPERVISING COMMITTEE:

Supervisor:

Bjorn Manuel Hegelich

John Keto

Pulsed photoneutron source driven by electrons from laser wakefield acceleration

by

Xuejing Jiao

Thesis

Presented to the Faculty of the Graduate School of

The University of Texas at Austin

in Partial Fulfillment

of the Requirements

for the Degree of

MASTER OF ARTS

The University of Texas at Austin

December 2017

Acknowledgements

I would like to express my deepest gratitude to my supervisor professor Bjorn Manuel Hegelich for his support in this thesis. A very special gratitude goes out to Joseph Shaw for his help in setting up and running the experiments and Tao Wang for his help in running the 2-D PIC simulation. I am grateful for the help and advice I received from Xiaoming Wang, Hai-En Tsai, Philippe Poth, Ishay Pomerantz, Lance Labun, Toma Toncian. It is my pleasure to work with these very talented people. I also want to thank Sarah Strigler, who taught me a lot in academic writing and helped me review this thesis. Last, I want to thank professor Mike Downer and Texas Advanced Computing Center for their generous permission to use their resource.

Abstract

Pulsed photoneutron source driven by electrons from laser wakefield acceleration

Xuejing Jiao, M.A.

The University of Texas at Austin, 2017

Supervisor: Bjorn Manuel Hegelich

Relativistic electron beams driven by laser wakefield acceleration (LWFA) were utilized to produce ultrashort neutron sources. The experiment was carried out on the 10 TW UT3, 38 fs, ~0.5 J, 800 nm Ti:Sapphire laser at the University of Texas at Austin. The target was a high-density pulsed gas jet composed of 90% Helium and 10% Nitrogen. The laser pulse with a peak intensity of $1.5\times10^{18}W/cm^2$ interacted with the target to create a cylindrical plasma channel of 60 um radius (FWHM) and 1.5 mm length (FWHM). Electron beams of ~80 pC with Gaussian energy distribution centered at $37MeV$ and a width of $30MeV$ (FWHM) were produced via laser wakefield acceleration. A 2D particle in cell (PIC) simulation was performed to study the acceleration process. The LWFA was found to be running at a nonlinear broken-wave regime. The electron spectrum acquired from simulation quantitatively agree with the experimental observation. Neutron fluence of $\sim2.4\times10^6$ per shot with ~300 ps temporal length was generated through bremsstrahlung and subsequent photoneutron reactions in a 26.6mm thick tungsten converter. Results were

compared with simulations in GEANT4, showing agreement in neutron fluence, neutron angular distribution and conversion ratio.

Table of Contents

List of Tables

List of Figures

Chapter 1: Introduction

1.1 Neutron Sources and Applications

Neutrons are charge neutral subatomic particles that were found by James Chadwick in 1932. Soon after the discovery, their practical value was realized and the first neutron radiography experiment was carried out in 1935 by H. Kallmann and E. Kuhn using a small neutron source (Bilheux, McGreevy, & Anderson, 2009). Over decades of research and development, more applications have been established. Now neutron sources are regularly used in a wide range of applications, including powder diffraction (Copley, 2001), petroleum exploration (Caldwell & Mills, 1959), neutron imaging (Bilheux et al., 2009), and neutron cancer therapy (Barth, Coderre, Vicente, & Blue, 2005). Some applications of the neutron source are very unique, making them an indispensable tool in research and industry.

Among these applications, neutron imaging is the most well-known technique. It is similar to x-ray imaging, both of which record 2D attenuation maps after penetrating objects with inner structures. However, the images produced by these two methods are quite different, mainly due to their different cross-section on different material. Figure 1.1 compares the cross-section between neutron beams and x-rays on common materials. It is obvious that x-rays are heavily attenuated in high-Z metals, where high electron density exists, and not so much on lighter materials. On the contrary, neutrons are scattered more by light materials and not so much in heavy metals, meaning that neutrons can deeply penetrate metals. This is the reason why they were utilized in metal parts inspection where x-ray imaging fails. The same property enables them to play a role in powder diffraction alongside x-ray powder diffractions. Both diffraction techniques provide diffraction

patterns to reveal the structure information of the material, but the different technique is preferred when comes to different materials.

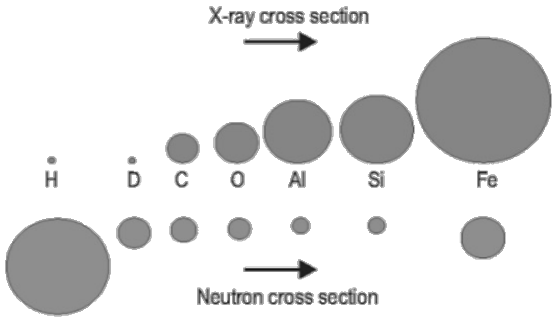

Figure 1.1: Comparison of cross-sections between neutrons and x-rays

Neutron sources are categorized by neutron energy spectrum, neutron flux, size of the source, etc. The most important parameter is the neutron flux, which is also characterized in different ways according to the applications. For example, in powder diffraction, mono-energetic neutron flux is required, so the neutron flux is reported in the unit of neutrons per wavelength per area per second. Neutron sources can also be classified into three types according to their energies, namely cold neutron sources, thermal neutron sources and fast neutron sources. Thermal neutron sources are the most widely used neutron sources, which are routinely employed in neutron powder diffraction and neutron imaging. On the other hand, active interrogation uses fast neutrons and neutron interferometer uses cold neutrons.

1.2 Traditional Neutron Source

Although, neutrons have many applications, there are not many ways they can be generated, unlike light source. In fact, only two types of high flux neutron sources are available. One is nuclear fission sources (Taylor et al., 2007) from nuclear reactors, which

exploit the most famous fission chain reactions. In the reactors, U-235 absorbs thermal neutrons and undergoes a fission process to give 3 more neutrons. These neutrons would, in turn, trigger more fission reactions after being slowed down in moderators. Then, the excessive neutrons in the reactors are guided out and serve as neutron sources. Neutron sources of this type include High Flux Isotope Reactor (HFIR) at Oak Ridge National Laboratory and ILL in France.

The other is spallation neutron sources (Taylor et al., 2007). To create this type of neutron sources, first, protons are accelerated using synchrotrons or linear accelerators to very high energies. Then these high-energy protons are directed to impinge on a heavy metal target and trigger spallation reactions. The heavy metal nuclei inside the target, bombarded by these high energy protons, disassemble into small pieces and ejects tens of neutrons. Typically, protons of energy around ~GeV level are used to blast the heavy nuclei, like Tungsten and Uranium. For each 1 GeV proton, 20~30 neutrons can be produced. Examples include the famous Spallation Neutron Source (SNS) in Oak Ridge and the ISIS in the UK. Of course, fusion reactions can also be used to produce neutrons, particularly Deuterium-Tritium (DT) fusion and Deuterium-Deuterium (DD) fusion, like that in the National Ignition Facility (NIF) and the ITER in France. However, none of them are currently being used as neutron sources due to the difficulty in controlling fusion reactions. All three types of neutron are summarized in table 1.1.

Type of source	Fission Source	Spallation Source	Fusion Source
Reactions	$n + {}^{235}U \rightarrow {}^{141}Ba + {}^{92}Kr + 3n$	$GeV\ p + heavy\ nuclus \rightarrow 20 \sim 30n + fragments$	${}^{2}D + {}^{3}T \rightarrow {}^{4}He + {}^{1}n$ ${}^{2}D + {}^{2}D \rightarrow {}^{3}He + {}^{1}n$
Operation Mode	Continuous	Continuous/Pulsed	Continuous/Pulsed
Average Flux	$\sim 10^{15} n/s$	$\sim 10^{17} n/s$	Not for practical use
Examples	HFIR(US), ILL(France)	SNS(US), ISIS(UK)	NIF(US), ITER(France)

Table 1.1: Summary of different types of high flux neutron sources

1.3 LASER-DRIVEN NEUTRON SOURCE

While national laboratory-scale neutron sources do produce a high neutron flux, they are huge, costly and sometimes even policy-restricted, which results in limited availability around the world (Bilheux et al., 2009). The development of tabletop particle sources based on high-intensity lasers has opened a window for laser plasma neutron source research. Laser-based neutron sources are of special interest because the laser plasma interaction has acceleration gradient thousands of times greater than conventional accelerators (Esarey, Schroeder, & Leemans, 2009; Macchi, Borghesi, & Passoni, 2013), whose accelerating gradients are limited to 100 MV/m partly due to the break down of the chamber material under strong electric field. The high acceleration gradient implies that to accelerate particles to the same energy level, laser plasma accelerator only need one-thousandth of the acceleration length, giving these sources the potential to be compact and portable. Moreover, laser-based neutron sources can also be versatile - from the same laser facility, users can obtain high energy electron beams (Wang et al., 2013), ion beams (Macchi et al., 2013), x-rays (Tsai et al., 2015) and neutrons (Pomerantz et al., 2014), all of which have unique applications in industry and research.

Most importantly, laser-driven neutron sources have a very short temporal structure and high peak fluence (Pomerantz et al., 2014). These features are favored by a

considerable amount of research and applications that employ pulsed neutron sources. For example, ultra-high neutron flux enables researchers to observe rapid neutron capture process (r-process) in laboratories, which was assumed to be responsible for the creation of heavy elements in the universe according to some research (Freiburghaus, Rosswog, & Thielemann, 1999). Another example is the fast neutron resonance radiography (FNRR) (Dangendorf et al., 2009). FNRR is an imaging method that can directly identify light elements by using their characteristic cross-sections resonance peaks. In this method, a broad-spectrum neutron beam is sent to pass through objects. The transmitted neutron spectrum is then modified and shows dips corresponding to these cross-section resonance peaks. By measuring the transmission spectrum using the n-TOF technique with spatial resolution, the information of elemental composition of the object can be acquired as well as the profile of the object. This method can determine the identity and density distribution of light elements simultaneously. However, this technique demands very short neutron pulses, preferably less than 1 ns. When using n-TOF to determine the energy spectrum, less uncertainty at neutron birth time can result in more accurate energy measurement, thereby enabling researchers to distinguish tightly spaced resonance peaks.

Figure 1.2 shows the general neutron generation schemes and challenges for laser-based neutron sources. The general scheme can be divided into three steps. The first step is to produce high energy particles using laser-plasma acceleration. Problems at this stage include optimizing particle beam, increasing laser repetition rate, and reducing the size of the laser. The second step is utilizing the high energy particles to generate neutrons. The challenges at this stage include choosing a suitable neutron generation scheme and engineering converters for optimal neutron yield. The third step is neutron detection or characterization, which essentially gather feedback on the performance of first two steps.

Generated neutron sources need to be monitored in order to evaluate the performance and further improve the yield, flux, and energy.

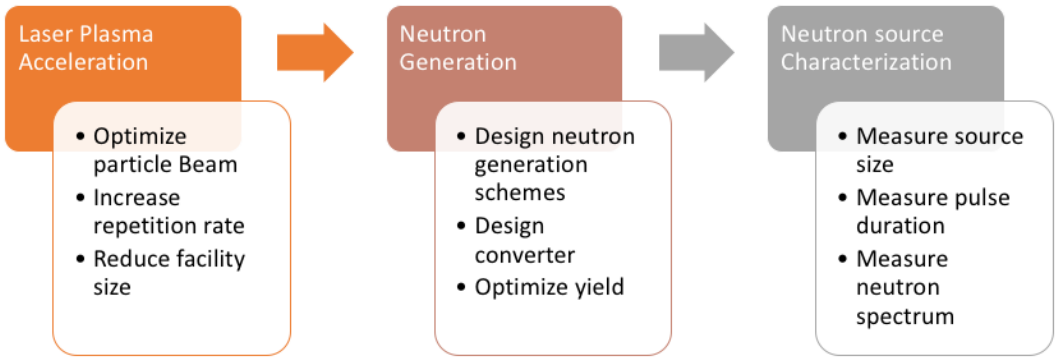

Figure 1.2: General scheme and challenges for laser based neutron source

Based on the scheme, several methods have been used to create neutrons from laser-plasma interactions. One method is to use laser-accelerated ion beams, usually protons or deuterons via target normal sheath acceleration (TNSA) (Wilks et al., 2001) or breakout afterburner mechanism (BOA) (Hegelich et al., 2013), to impinge on a converter made of a material of a high cross-section for neutrons generation, for example, deuterium (Willingale et al., 2011), beryllium-9 (Jung et al., 2013; Roth et al., 2013, 2016), and lithium-7 (Lancaster et al., 2004). Normally, proton acceleration is conducted by a focusing high-intensity laser to a tiny spot on the surface of a thin metal foil and ionizing the foil instantaneously and create a tiny spot of hot plasma. Electrons, absorbing most of the laser energy, expand much faster than the ions due to their light mass. These energetic electrons, when escaping from the back surface of the target, create an electron sheath field and accelerated ions in that field. This is known as the target normal sheath acceleration (TNSA) mechanism. The newly discovered regime breakout after burner (BOA) utilize very thin targets, which are volumetrically heated during laser shots. In BOA regime, laser

pulses can propagate through the thin foil targets and directly accelerate ions due to relativistic effect. This process was found to be more efficient than the TNSA mechanism and also have superior performance in generating neutrons (Hegelich et al., 2013). However, to reach this regime is not always easy because of the requirement for very high contrast laser pulses.

The second method is to shoot high-intensity lasers on deuteron gas targets (Ditmire et al., 1999) or deuterated bulk targets with or without a deuterated converter (Willingale et al., 2011). This scheme is also known as inertial confinement fusion. In this process, energy was gained from the laser by the ions to overcome the Coulomb barrier and trigger fusion reactions. This process usually yields a much lower neutron flux due to the very limited reaction volume.

The last method is to irradiate the converter with high energy electron beams (Gupta & Suk, 2007) that are generated from laser wake field acceleration (LWFA) (Esarey et al., 2009) or direct laser acceleration. In this method, multi-tens of MeV electrons are sent to the converter usually made of high-Z materials. High energy electrons scatter in the converter by the nuclei and radiate bremsstrahlung γ-rays of energy up to the same energy of electrons. The γ-rays that have energies higher than the nuclear binding energy will be absorbed by the nucleus, inducing photoneutron reactions and release neutrons form the nuclei.

Laser-driven neutron sources are still an ongoing research and also an important topic because of their unique applications in a lot of areas (Taylor et al., 2007). Research is being conducted to find a way to provide cheap, portable and high flux neutron source for academia and industry. In this thesis, an experiment is reported, in which neutron yield from LWFA was optimized by varying the target content, density, and converter material. This experiment was performed at the UT3 laser lab, a TW class 800 nm laser, at the

University of Texas at Austin. The results were found to be superior to most of the previous results on the same laser scale.

Chapter 2: Experiment Principle

1.1 Experimental scheme

This experiment utilizes relativistic electrons from the laser-plasma acceleration to generate fast neutrons. The physics process involved here can be concisely presented in Figure 2.1. First, a high-intensity laser was focused on a gas jet target that made of low-Z inert gas. The laser pulse ionizes the gas target as it passing through and accelerate electrons though Laser Wakefield Acceleration (LWFA). Then, the multi-tens of MeV electrons were directed to incident on a tungsten converter, in which electrons decelerate by the heavy nuclei and radiate high energy γ-rays, known as bremsstrahlung radiation. High energy γ-rays (> 6 MeV) have certain probabilities to trigger photon activated nuclear reactions and eject neutrons out of the nuclei.

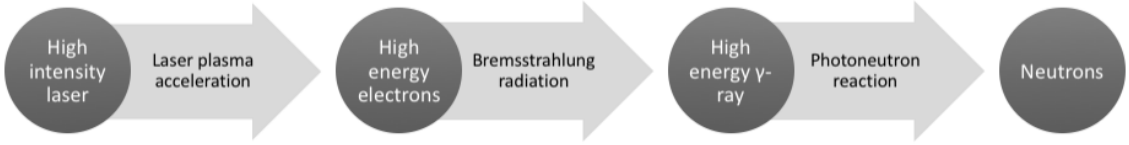

Figure 2.1: General scheme of the experiment

1.2 Laser Wakefield Acceleration

By far, LWFA is the most explored and effective laser electron acceleration mechanism. It was proposed by Tajima and Dawson in 1979 (Tajima & Dawson, 1979). The standard LWFA is driven by a single, short laser pulse of very high intensity in underdense plasma. When a high-intensity laser pulse ($> 10^{17} W/cm^2$) shooting into a gas target, the electric field of the laser pulse will suppress the nuclear electric field in atoms

and free electrons from their bounded state, a process known as barrier-suppression ionization. Essentially, gas targets can be thought as fully ionized plasma when dealing with high-intensity lasers (even though not necessarily all electrons are ionized).

Plasmas generally do not contain strong electric fields due to the Debye shielding, so they can be considered in a quasi-neutral position. When the electrons inside the plasma departed from their quasi-neutral position, they are subject to an electric force due to this deviation. Just like an object attached to a spring, electrons depart from its equilibrium point will also oscillate around their stable positions. By solving the Newtonian equation, the electrons oscillation frequency can be easily found to be

$$\omega_p = \sqrt{\frac{n_e e^2}{m_e \epsilon_0}}$$

where n_e is electron density, m_e is the electron mass, and ϵ_0 is the vacuum permittivity.

The critical density n_c is defined by setting the plasma frequency ω_p equals to the laser frequency ω. If the electron density exceeds the critical density, the refractive index of the laser in plasma becomes an imaginary number, which translates into diminishing electromagnetic waves. In other words, laser pulses cannot propagate in plasma that has a density higher than the critical density. Therefore, plasma denser than the critical density is called overdense plasma and the one that below this density is called underdense plasma. In this experiment, the critical density for 800 nm Ti: Sapphire laser is $1.7\times10^{21}/cm^3$, which far exceeded the normal gas density. In fact, all of the LWFAs were run in underdense plasmas.

When a laser pulse propagates in an underdense plasma, the electric field of the laser pulse applies electric forces on the charged particles and force them to move. Ion movement was neglected because the time scale for ions to respond is much longer than

the laser-plasma interaction due to the heavy mass of the ions. Since the electric field inside the laser pulse is oscillatory, the electrons in the laser field then also oscillate at the same frequency as the laser optical frequency. In addition to this normal electric force, the intensity difference inside the laser pulse implies the existence of variances in the electric field amplitudes. The inhomogeneity in the amplitudes has collective effects on the electrons, which tends to push electrons along the negative gradient of the intensity, much like the force exerting on particles from a conservative potential field. Thus, they are described as ponderomotive potential and ponderomotive force. The expression of ponderomotive force can be derived by solving the electron fluid momentum equations in the cold plasma limit and is shown below

$$F_p = -\frac{e^2}{4m\omega^2}\nabla(E^2)$$

where F_p is the ponderomotive force, e is the charge of the particle, m is the electron mass, ω is the optical frequency the field, and E is the amplitude of the electric field. The magnetic field is neglected in this case because it exerts very little force on the particles compare to the electric force.

One of the implications of the ponderomotive force is that high-intensity laser pulses are able to expel a large number of electrons from their envelope when they are propagating through the ionized gas and therefore excite large-amplitude Langmuir waves in plasma behind them, known as the laser wakefield. Strong electrostatic field is created inside the wakefield due to space charge separation. Electrons trapped inside the wake can be accelerated by the electrostatic field. Accelerated electrons can move with the laser wakefield, which in turn moves at the speed close to the speed of light, and continually being accelerated until dephasing or depletion of the laser energy. It has been demonstrated that the LWFA is driven most efficiently near resonance (Esarey et al., 2009), which is

when the laser pulse length L is on the order of the plasma wavelength λp. This is the exact condition which guides the electron acceleration in this experiment.

1.3 Electron Interact with Matter

When high energy electrons enter a medium, they interact with the electrons and nuclei in the medium and slow down as they are penetrating into the material. Because of the light mass of the electrons, the matter can be considered as composed of loosely bounded electron cloud around almost immobile nuclei, both of which are charged particles. The interactions can be viewed as binary collisions conducted through electromagnetic force between the energetic electrons with either the bounded electrons or nuclei. The energy transfer from the incoming electrons to the medium or radiation was characterized by stopping power, which is defined as energy loss per unit travel distance. Generally, there are two types of stopping power. One caused by electrons and is called collisional stopping power. The other caused by nuclei, known as radiative stopping power.

Collisional stopping power is a result of collisions between the high energy electrons and the bounded electrons. In this collision, a considerable amount of the energy can be transferred because of the comparable mass of these two particles. The energy gain by the bounded electrons during the collision will help them escape from the nuclear coulomb potential and move freely in the matter. Sometimes, the freed electrons can have enough energy to travel a significant distance and produce further reactions just as the primary electrons. This process will continue until the energies of the free electrons are too small to cause further ionization. Energy loss due to collisional interactions eventually becomes thermal energy.

On the other hand, electrons can also interact with the nuclei, whether they are primary electrons or secondary delta rays. When they do so, due to the big mass difference

between the two particles, instead of losing energy to the nucleus, the energy was lost mainly due to radiation of high energy photons (γ-rays), called bremsstrahlung radiation. The amount of bremsstrahlung radiation yield depends on the energy of the incoming electrons as well as the material and composition of the matter. The radiative stopping power can be estimated by using the formula shown below

$$-(\frac{dE}{dx})_r = \frac{NEZ(Z+1)e^4}{137m_0^2c^4}(4ln\frac{2E}{m_0c^2} - \frac{4}{3})$$

where E is the energy of the electron, N is the atomic number density, Z is the atomic number, m_0 is the electron mass, c is the speed of light. The higher the atomic number (Z-number) of the material, the better the capability it can produce bremsstrahlung radiation. This relation scales as $\sim Z^2$. The ability to generating bremsstrahlung radiation is also proportional to the electron energy E. Figure 2.2 (a) shows the energy dependence of the bremsstrahlung radiation yield ratio on different materials, which is defined as E_{rad}/E_{total}. It is obvious that the higher the electron energy, the higher Z number of the converter material, the more energy lost to bremsstrahlung radiation. Figure 2.2 (b) shows the collision mass stopping power and radiative mass stopping power for different materials at the different energy level. The collision stopping power does not vary much for electrons with energy above 10 MeV, while the radiative stopping power strongly depends on the electron energy. Both graphs indicate that to effectively generate neutrons, high Z materials need to be adopted and the energy of electrons need to be at least above 30 MeV.

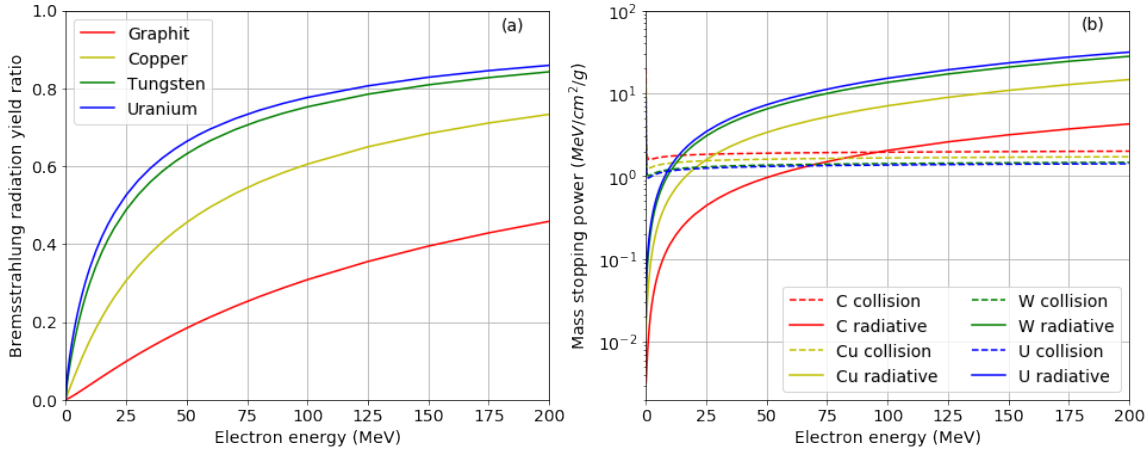

Figure 2.2: (a) Energy dependence of bremsstrahlung radiation yield ratio on different materials. (b) Collision stopping and radiative stopping power for carbon (C), copper (Cu), tungsten (W) and uranium (U). Data was taken from National Institute of Standards and Technology (NIST) ESTAR database.

1.4 Photon Interact with Matter

After producing γ-rays from the radiative interaction between electrons and nuclei, the next step is to apply these γ-rays to produce neutrons. However, a lot of interactions can happen as well when γ-rays incident into matters. These interactions include photoelectric effect, photonuclear reaction, Compton scattering, and pair production, as shown in Figure 2.3. The photoelectric effect is the phenomenon that a bounded electron is ejected from the atom after absorbing a photon. Compton scattering is an inelastic collision between the incident photon with an electron. According to special relativity, high energy photons have masses as well as momentums. They can be treated effectively as normal charge neutral particles that can participate in electromagnetic interactions. In order for Compton scattering to happen, the photon mass/energy should be at least the same order of the rest mass energy of an electron, which is 511 keV. When a photon energy is more than twice the rest mass energy of an electron, it can convert into an electron-positron pair in the electric field near the nucleus, known as pair production.

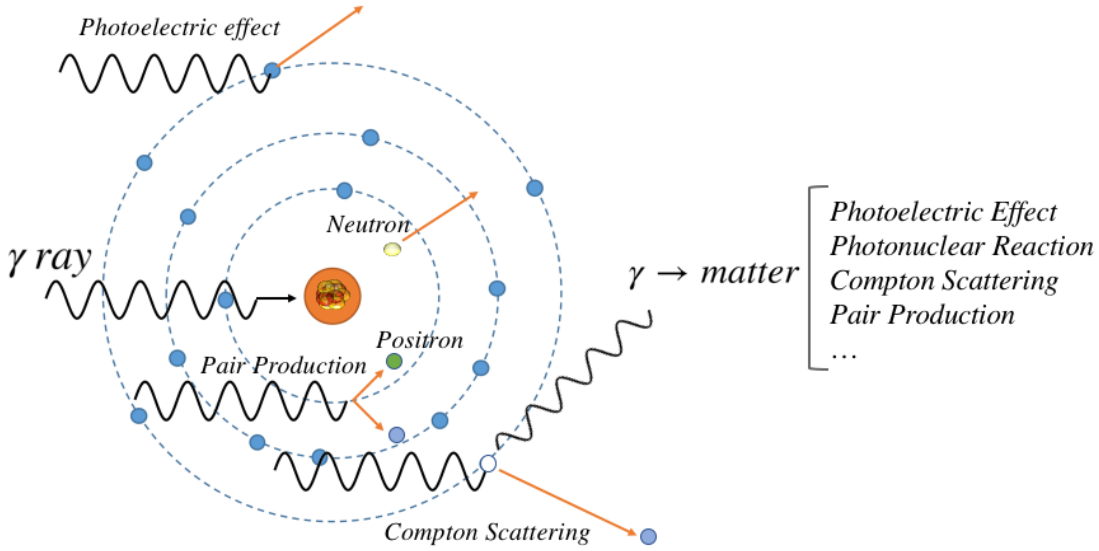

Figure 2.3: Illustration of photon interact with matter

Figure 2.4 illustrates the regime in which each reaction dominates. All three effects can occur during the interaction but only one of the reactions dominate at a given situation. The relative intensities of these reactions are affected by the atomic number of the absorber as well as incidental γ-ray energies. The green line in Figure 2.4 corresponds to the state where the cross-sections of two different reactions are equal. The photoelectric effect is the dominant reaction at high-Z materials and low photon energy. Compton scattering is the dominant reaction in low-Z materials for photon energy at ~MeV level. Pair production dominates at high-Z materials with high energy γ-rays. In this experiment, nuclear binding energy for tungsten is above 6 MeV, so the most prominent competing reaction is pair production.

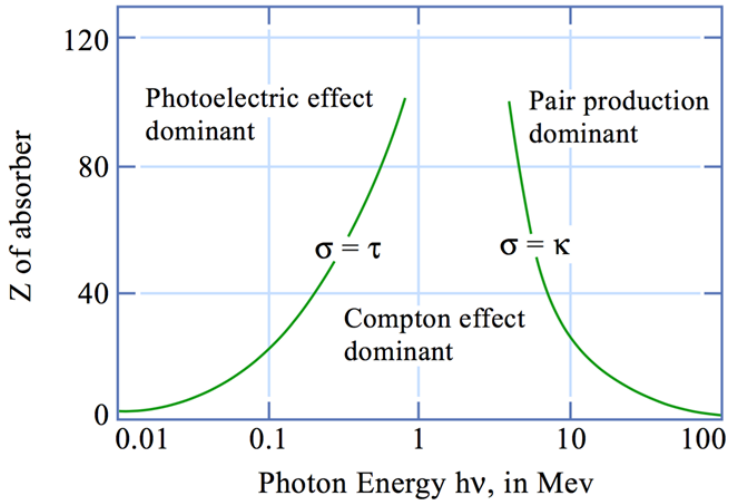

Figure 2.4: Diagram of the dominance for each γ-ray reaction in matter. Image credit: MIT OCW

The last interaction discussed here is photonuclear interaction. In rare cases, photons with energy exceed the nuclear binding energy flying towards the nucleus will be absorbed. The nucleus then enters into an excited state, which usually immediately decays to release the excess energy by emitting subatomic particles, for example, neutrons, alpha particles etc. Photoneutron reaction is one type of photonuclear reactions, in which neutrons are emitted. The reason that it is not shown in above diagram is that it is not as significant compared to other interaction channels. Photoneutron reaction also strongly depends on materials because of the different nuclear inner structures. Nevertheless, this reaction is the concern of this experiment. Figure 2.5 shows the photoneutron cross-section for uranium-238 (depleted uranium) and tungsten (W182, W183, and W186). For uranium, the peak cross-section occurs at 14 MeV and is roughly 300 mb. For tungsten, their cross-section peak around 13MeV and 450 mb, making tungsten a better option for converter material.

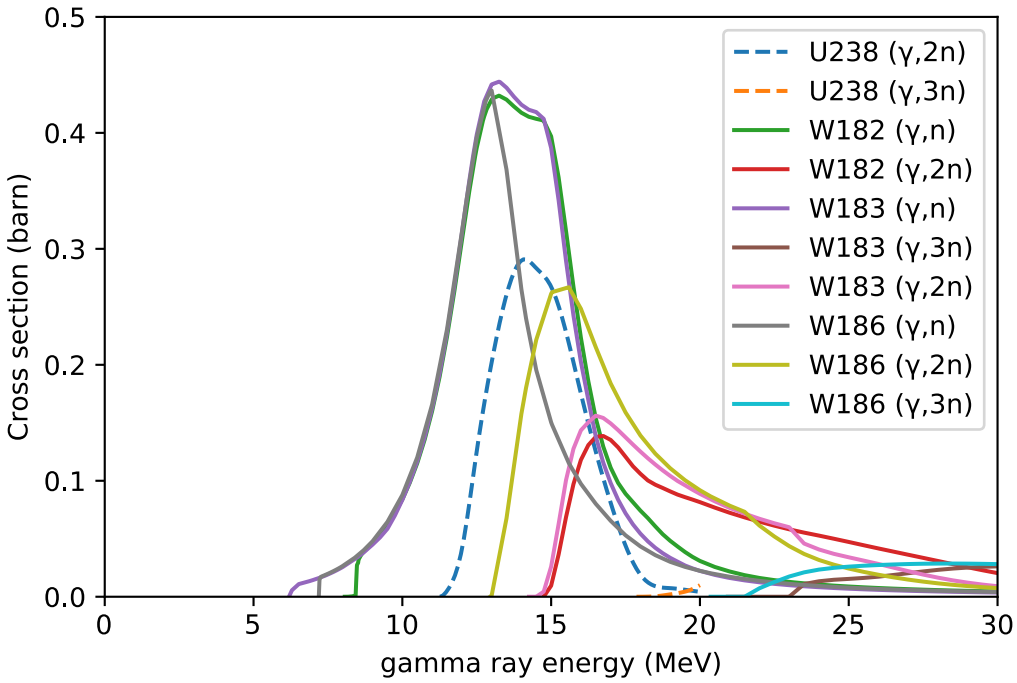

Figure 2.5: Photoneutron cross-section for uranium-238 and tungsten isotopes.

The converter design is critical in increasing neutron flux and requires a deep understanding of the interaction between radiation and matter. A high photoneutron absorption cross-section can help increase neutron yield and reduce the converter size, yielding a shorter neutron pulse and higher surface flux. However, what actually affects the conversion efficiency is the ratio of photoneutron cross-section over the total inelastic cross-section, which includes pair productions, Compton scatterings, and other photonuclear reactions, but this still has not told the whole story because of the existing secondary reaction channels. For example, high energy electrons from Compton scattering can further induce γ-rays or delta rays. These cascading reactions obscured the problem. Sometimes, the subatomic particles from photonuclear reaction can interact with stable nuclei as well. For example, fast neutrons can be absorbed by U-238. Therefore, the

converter structure, material, and size need to be carefully designed with the aid of computer simulations.

Chapter 3: Experimental Setup[1]

3.1 Experiment Overview and Layout

The experiment was designed based on the UT3 laser system at the University of Texas at Austin. UT3 is a TW class Ti:Sapphire laser with a central wavelength of 800 nm, which can operate at a repetition rate of 10 Hz. The general schemes of this experiment are shown in Figure 3.1. To generate LWFA, 38 fs, ~ 0.5 J, linearly polarized laser pulses were focused to a spot of ~17 μm (FWHM) with a peak intensity of $1.5\times10^{18}W/cm^2$. The energy and fluence of the electron beams that are suitable for maximizing neutron production were controlled by the plasma density, which is in turn controlled by the gas type and density. The gas target was composed of 90% He and 10% Nitrogen to provide more electron injection in LWFA. The gas jet nozzle has a 3×1 mm rectangular opening with 1 mm axis aligned with laser propagation direction. A transverse interferometer measured the time-averaged plasma density profile. A removable electron spectrometer was used to monitor the electron beam spectrum by dispersing the electrons on a LANEX screen. The LANEX image plate was also used to monitor the original beam divergence and calculate the total electron fluence when both magnetic field and converter are absent. When generating neutrons, a tungsten converter was placed behind the gas jet target to catch all the high energy electrons. The neutron fluence was monitored by bubble detectors and a neutron Time of Flight (n-TOF) detectors. The n-TOF was also used to measure the spectrum of neutrons by accumulating a considerable amount of laser shots.

---

[1] Part of the content in this chapter based on the article *Jiao et al., "A Tabletop, Ultrashort Pulse Photoneutron Source Driven by Electrons from Laser Wakefield Acceleration."*. The author of this thesis designed the experiment, collected and analyzed the data, ran the simulations, wrote the paper and made the figures for the article.

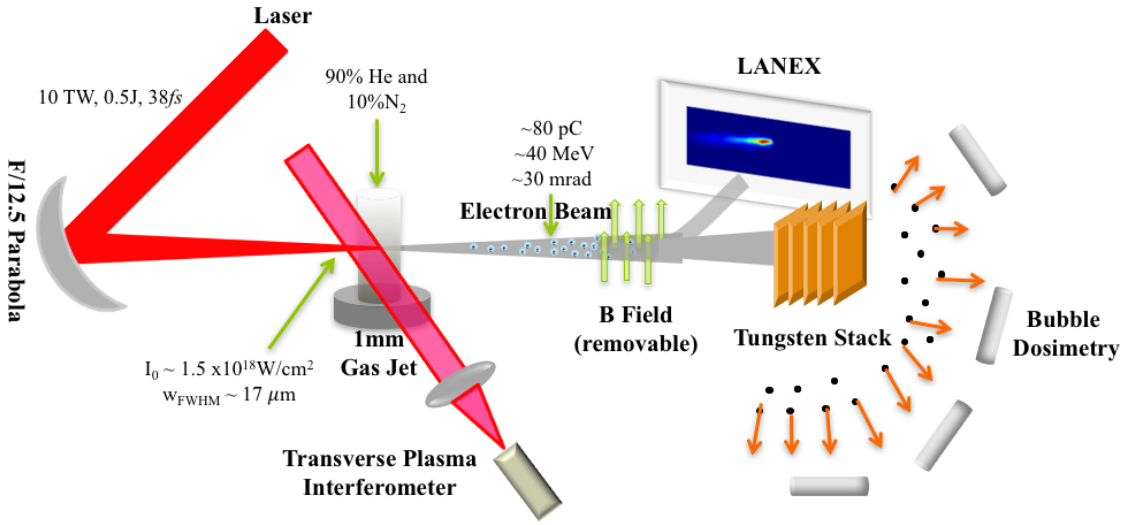

Figure 3.1: Illustration of the experimental scheme.

The vacuum chamber layout is shown in Figure 3.2. The main beam, shown in red, entering from the right side of the chamber, was collimated through a pair of mirrors and focused on the gas jet target through a F/12.5 off-axis parabola (OAP). The focusing position was determined by a thin metal wire taped at the front edge of the gas jet. The probe beam used for the plasma interferometer was separated from the main beam outside of the chamber and sent in through another flange. Either a tungsten converter or a magnetic electron spectrometer was placed on the beam axis after the gas jet target as shown in the layout. The magnetically dispersed electrons by the electron spectrometer were imaged by a LANEX screen and recorded by a 12 bit CCD camera. The front surface of LANEX screen was warped in a thin aluminum foil to block the laser light. The back surface of the LANEX screen was imaged by the CCD camera outside the chamber. The whole LANEX and CCD imaging system was shielded in a small aluminum compartment to avoid the interference of visible light generated inside the chamber. Five bubble detectors were

deployed around the chamber as shown in Figure 3.2, which were used to measure the neutron fluence. A neutron Time-of-Flight (n-TOF) was placed 2.18m away from the converter and at ~50 degrees from laser propagation direction as shown in Figure 3.2.

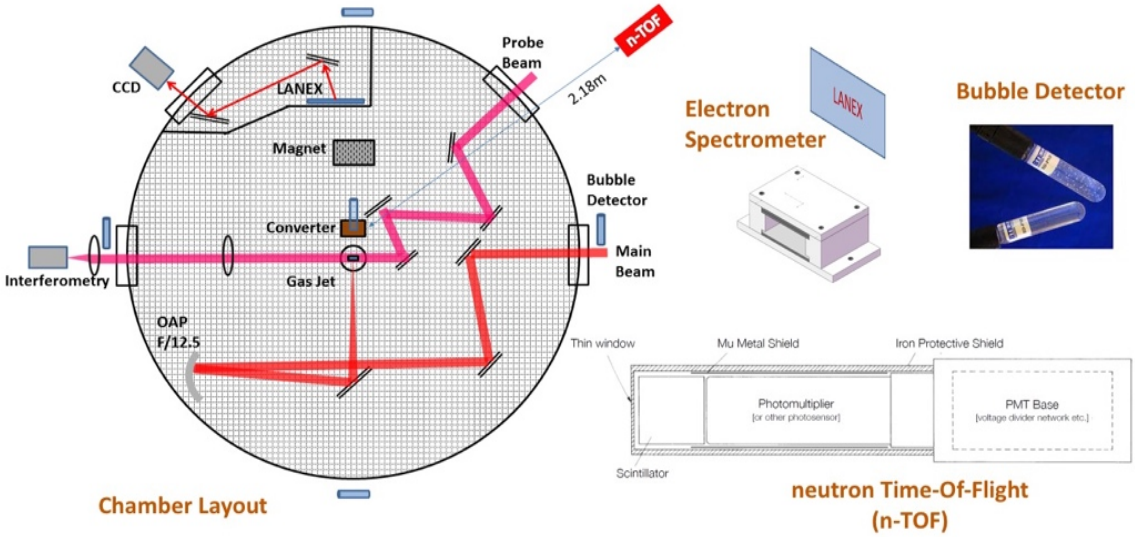

Figure 3.2: Left: chamber layout of the experiment was shown on the left. Right: illustrations of diagnostic equipment: electron spectrometer, bubble detectors, neutron Time of Flight detector.

3.2 Plasma Interferometer

Interferometry is a technique that uses the interference property of two coherent electromagnetic waves. The change of the optical path length caused either by refractive index change or geometrical difference results in a phase change in the beam. The phase change carried by the probe beam can be recorded through an interferogram fringe after the probe beam was superimposed by an undisturbed reference beam. The phase shift information can then be extracted by analyzing the fringe shift. Plasma interferometry has been widely used in the study of laser plasmas interaction, especially in LWFA, where the interaction happened in underdense plasma which facilitates the use of this technique.

Plasma interferometer can provide information of a two-dimensional phase shift in the transverse plane of the probe beam. The phase shift is controlled by both the geometrical profile of the plasma and local refractive index as shown in Figure 3.3. The refractive index of plasma related to the electron density through the following equation

$$\eta = \sqrt{1 - \frac{n_e}{n_c}}$$

where η is the refractive index, n_e is the electron density, n_c is the critical density. After assuming a cylindrical symmetry along the laser direction, which is perpendicular to the probe beam, 3D electron density profile can be calculated the by using the 2D phase shift map and the Abel inversion formula that shown below

$$n_e(r) = \frac{\lambda n_c}{\pi^2} \int_x^{r_0} \frac{1}{\sqrt{r^2 - x^2}} \frac{d\phi(x)}{dx} dr$$

where λ is the wavelength of the probe beam, r is the radius of the plasma profile, $\phi(x)$ is the phase shift along the x-direction.

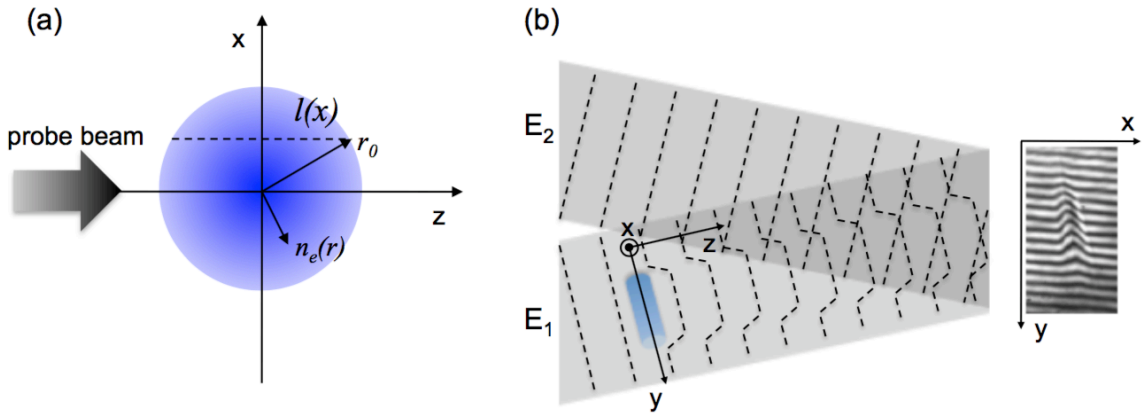

Figure 3.3: (a) Illustration of the plasma interferometer, where cylindrical symmetry was assumed along the laser propagation direction (y-axis). The probe laser transversely passes through the plasma and experience a phase shift depend on the plasma density and profile. (b) Illustration of the formation of interferogram after two beams overlaps, one is phase shifted probe, the other is the undisturbed reference beam. Image credit: Hai-En Tsai

In the experiment, the plasma interferometry was set up by splitting the probe beam from the main beam which ensured a relative stable time synchronization. The time synchronization was fine-tuned by using an optical delay stage. Because of the nature of superfast interaction, the accuracy of the time synchronization between the main beam and probe beam need to agree in the picosecond level in order to capture the interaction. Another difficulty is to acquire a stable interferogram. The coherence length of the probe is only 11 μm, so it is very challenge to overlap the reference beam with the probe beam if the beam paths are different, because vibration along different routes are likely bigger than the coherence length. In the experiment, the probe beam interfered with itself rather than a separated reference beam. This is realized by expanding the probe beam to make sure only a small portion of the beam passes through the plasma. The clean part of the probe was used as reference beam by separating the probe at the last stage with a 50/50 beam splitter and flipping the separated beam using a roof mirror.

3.3 Neutron Time of Flight Detector

Time of flight detection is the most widely used technique in determining neutron kinetic energy. The principle of how the neutron time of flight detector works is very simple. It measures the time that neutron takes from the original position to the detector. In the early days, n-TOF was made of mechanic chopper that can select certain neutron energy. Today, most of the n-TOF utilize scintillators with oscilloscopes. Plastic scintillators are the most commonly used detectors because they are rich in proton and relatively stable in property compare to other scintillators. Depending on the distance between the source and the detector, a TOF spectrometer can resolve neutron energies ranging from sub-MeV to hundreds of MeV. However, it can only be used to measure pulsed neutron source, since only pulsed neutron source has a definite starting time. In

most cases, the neutron energies measured are much smaller than their rest mass energy (940 MeV), so the relativistic effect can be neglected. Figure 3.2 illustrates how the n-TOF spectrometer works. The first part of the n-TOF is a quenched fast plastic scintillator, where fast neutrons can effectively create energetic recoil protons through elastic collisions. The energetic protons then deposit most of their energies through collision with electrons alone their pathway, resulting in the scintillators to emit light of certain wavelengths. The light signals are then amplified by photomultiplier (PMT) tubes and converted to electrical signals, which then recorded by oscilloscopes. For the n-TOF to accurately record the energy spectrum, the detector response time and signal spread need to be much shorter than the flying time of neutron. The photomultiplier used in this experiment is XP2020, which features in very short response time, low noise and excellent linearity. The scintillator used (EJ-232Q) also have short decay time of less than 1ns. Thus, the total response time for this system is less 6 ns and only contribute a small amount uncertainty to the measurement. The oscilloscope was trigger by the very strong γ-rays from the laser shot. In this experiment, n-TOF was also used to count neutron flux in addition to bubble detectors.

3.4 ELECTRON SPECTROMETER

Electron spectrometers are very standard devices to measures electron energies. The principle of the devices is based on the fact that a charged particle traveling in a magnetic field experiences a Lorentz force in the direction perpendicular to both the velocity and the magnetic field. The magnitude of the force depends on the charge and velocity of the particles. For electrons, the charges are always the same, so their trajectories are separated according to the velocities, therefore energies. The spread of electrons on the screen can be readily translated into energy spectrum by using a theoretically calculated calibration curve. The electron spectrometer used in this experiment was design by using

Radia software package (Chubar, Elleaume, & Chavanne, 1998) to measure electrons with energies specifically between 10-50 MeV. The spectrometer consists of two parts. The first part is the magnet assembly. The CAD model of the magnet assembly is shown in Figure 3.2. The white frame is the yolk made of stainless steel. The grey parts correspond to the NdFeB magnet. The second part of the electron spectrometer is the LENAX screen coupled with a 12-bit CCD camera. The LENAX screen was placed at a certain distance behind the magnet to increase the energy resolution. Another function of the LENAX and CCD camera system is to determine the charge and beam divergence when the magnet was not present. The absolute electron bunch number can be tracked back from the intensity of the CCD image after taking into account the quantum efficiency of the CCD chips, the collecting angle of the photon emitted from the screen, and the calibrations of the phosphor screen (PI200). The data for this calibration was published by Y.C. Wu on Review of Scientific Instruments (Wu, Zhu, Dong, Yan, & Gu, 2012). Figure 3.4 shows the measured magnetic field by using a gauss meter inside the device, where z-axis is the direction that the electrons inject. The electron trajectories calibration curve was calculated by tracking relativistic electron through the non-uniform magnetic field from the middle of the entrance.

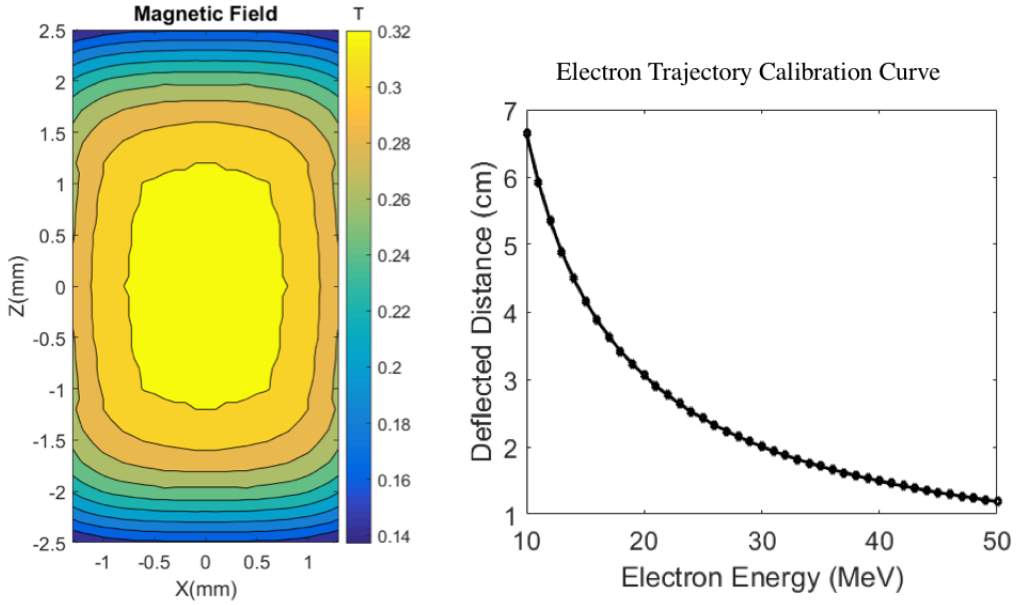

Figure 3.4: The contour plot of the magnetic field and electron trajectory calibration curve of the electron spectrometer

3.5 Bubble Detector

Bubble detectors (Ing, 2001) were used in the experiment for measuring neutron fluence. The principle of bubble detectors resembles bubble chambers. However, the neutrons carry no charge, so they cannot interact with other matters and cause ionization events like that in the bubble chamber. For thermal and slow neutrons, Boron-10, Lithium-6, or Helium-3 was often used to absorb the neutrons and produce γ-rays or alpha particles, which can then be readily detected as electric signals. Fast neutrons have a low absorption cross-section in most medium. The only efficient way to detect fast neutrons is to through elastic scattering between a neutron and a lightweight nucleus. Bubble detectors are composed of droplets of superheated liquid, where neutrons can deposit energy through elastic collisions with nuclei and cause the droplets to vaporize and form visible bubbles. Apart from being very sensitive to neutrons, bubble detectors almost never respond to γ-

rays and the neutron sensitivity is independent of neutron dose rate and energy, both of which are very desirable features in laser-plasma experiments. The bubble detectors used in this experiment have a sensitivity above 30 bubbles/mrem. Nevertheless, this sensitivity is still too small to see a consistent signal in one laser shot. Instead, two hundred of shots was accumulated to acquire an accurate average yield.

Chapter 4: Results and Simulation Analysis[2]

4.1 Plasma Density

Plasma density was recorded for all the shots to help optimize the electron beam. The plasma density profiles were found to be consistent from shot to shot under the same target and laser conditions. The laser was focused on the front edge of the gas jet and created a cylindrical plasma channel of 60 μm in radius and 1.5 mm long (FWHM). Figure 4.1 shows the typical plasma density measured when generating neutrons, including the source image as well as the calculated final density profile. The phase shift was calculated by comparing the source fringe with the prerecorded background and then, the density profile was extracted by using Abel inversion. The highest plasma density was found to be $3.5\times10^{19}/cm^3$.

[2] Part of the content in this chapter based on the article *Jiao et al., "A Tabletop, Ultrashort Pulse Photoneutron Source Driven by Electrons from Laser Wakefield Acceleration."*. The author of this thesis designed the experiment, collected and analyzed the data, ran the simulations, wrote the paper and made the figures for the article.

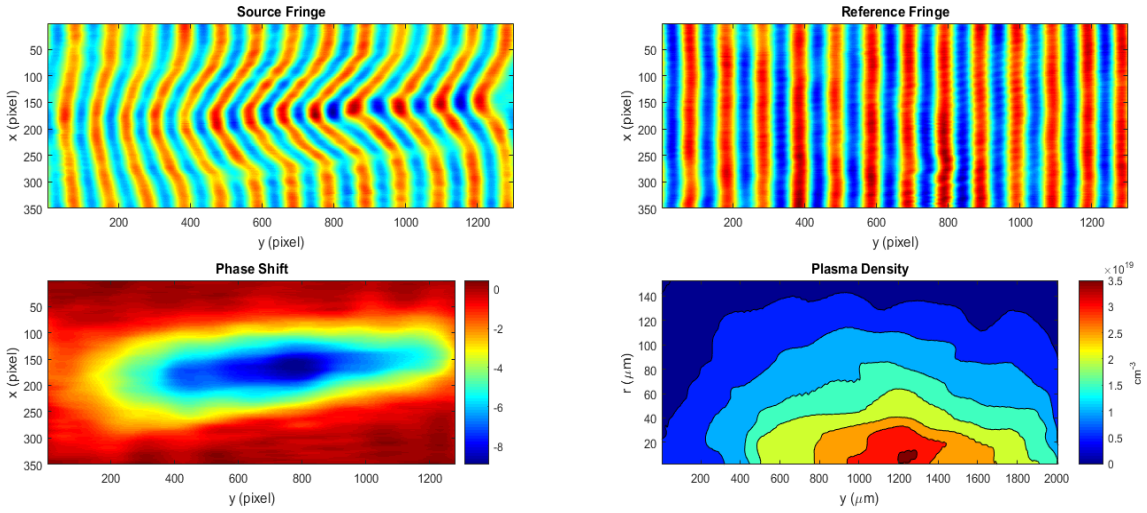

Figure 4.1: Top: images of source fringe and background fringe. Bottom: the calculated phase shift and the contour plot of the plasma density.

4.2 Electron Beam Diagnostic

The electron beam generated through LWFA in this experiment had a low divergence with FWHM of 30 mrad, which made online electron measurement almost impossible, so the electron beam properties were analyzed and optimized before the converter was inserted. The image on the left of Figure 4.2 is the electron spot intensity image. A Gaussian fit estimates the electron beam divergence. The image on the right of Figure 4.2 is the averaged electron energy distribution from the electron spectrometer and the LANEX intensity images. The electron energy spectrum has an approximately Gaussian distribution with the energy peak at 37 MeV and width of 30 MeV (FWHM).

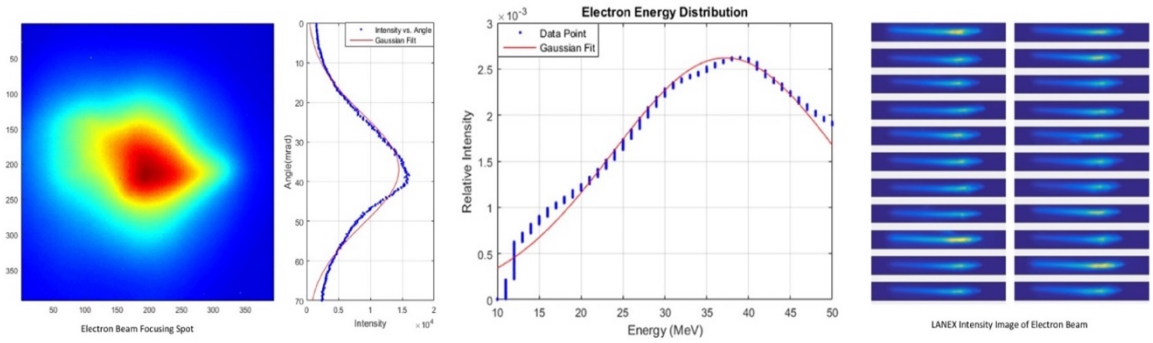

Figure 4.2: Left: electron beam image on the LANEX screen and Gaussian fit on the divergence profile; Right: averaged electron energy distribution and LANEX intensity images.

4.3 Particle In Cell Simulation

A 2D particle-in-cell simulation was performed with EPOCH code to investigate the acceleration mechanism. In the simulation, a Gaussian pulse of the same parameters propagated through a trapezoid-shape plasma profile with the maximum density of $3.5\times10^{19}/cm^3$. Figure 4.3 (a) shows the electron spectrum, which resembles a superposition of an exponential decrease at low energy with some tens of MeV peaks with energy around 30-40 MeV. Due to the limitation of the electron spectrometer, the low energy tail was not recorded, but the high-energy portion was found to qualitatively agree with the simulation. Figure 4.3 (b-d) reveals the evolution of the interaction. The normalized vector potential a_0 was ~0.8, indicating a mildly nonlinear interaction in the beginning. Then laser underwent a self-focusing process, resulting in a much bigger a_0, and eventually brought the interaction into a highly nonlinear broken-wave regime (Pukhov & Meyer-ter-Vehn, 2002). The wave breaking happened at 2.7 ps and electrons trapped in the first wave bucket was accelerated up to 60 MeV. It should be noted that although the ratio between laser pulse length L and the plasma wavelength λ_p was 2, self-modulated wakefield was not observed in the simulation.

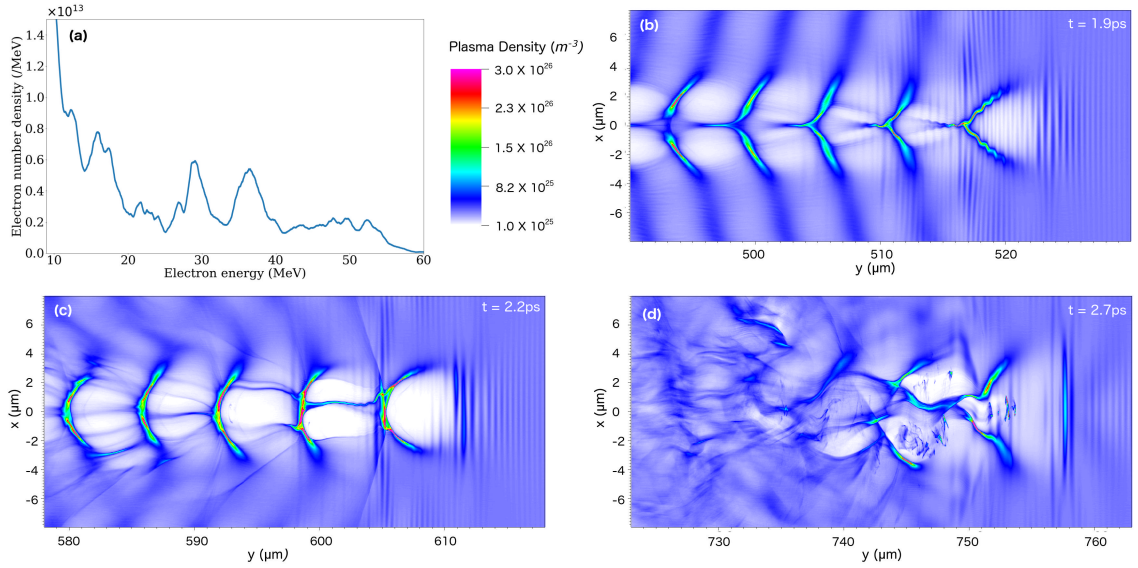

Figure 4.3: (a) Electron spectrum from the PIC simulation. (b-d) Electron density snapshots for t=1.9 ps, 2.2 ps, and 2.7 ps during the 2D PIC simulation.

4.4 Neutron Fluence and Spectrum

The neutron fluence was measured by 5 bubble detectors placed outside the chamber at 0, 90, 90 (at the top of chamber), 180 and 270 degrees with respect to the laser/electron propagation direction and respective distances of 50 cm, 60 cm, 46 cm, 69 cm and 60 cm from the converter target. Figure 4.4 shows the plot of the neutron fluence angular distribution on the left. The x-axis is the angle from laser propagation direction. The y-axis is neutron fluence in units of neutron number per sr. The bubble detector set at the top of the chamber was considered as 90 degrees in the plot and the fluence was very consistent with the detector on the side.

A nearly isotropic neutron fluence, except front direction, was observed. The reason for a much higher front fluence signal is due to some of the γ-rays passing through the converter and creating an additional source of electrons via Compton scattering and pair

production in the chamber wall. The forward bubble detector was very close to this electron source and thus saw a large fluence of direct electrons. The bubble detectors appeared to be sensitive to these electrons. More discussion will be given on this topic in the subsequent GEANT4 simulation section. This problem could be avoided and the neutron yield could be increased by using a thicker converter. However, this action will inevitably reduce the available neutrons and surface fluence due to the absorption in the converter and a bigger surface area. Data collected at other positions, which were not affected by γ-rays, demonstrates a neutron fluence of $> 2\times10^6$ neutrons per shot, a result higher than previous experiments on comparable laser systems.

The graph on the right of Figure 4.4 is the neutron energy distribution. Detecting neutron energy is challenging and commonly use time of flight method, which requires the detectors to be set far away from the neutron sources to accurately resolve the neutron energies. However, this practice also drastically reduces the signal level, so we accumulated 200 shots during the experiment using an n-TOF signal spread from 100 to 400 ns to determine the energy distribution. The energy distribution was calculated by differentiating the numeric fit of the accumulated signal. The average number of neutrons detected on each shot was approximately 1.2, obtained from the oscilloscope waveform counting. This number matches well with the total neutron fluence implied by the bubble detectors. In Figure 4.4 right, the blue dots show the accumulated neutron number received at the scintillator, and the red line is the numerical fit to this data, which is then used to find a smooth energy distribution, shown in yellow.

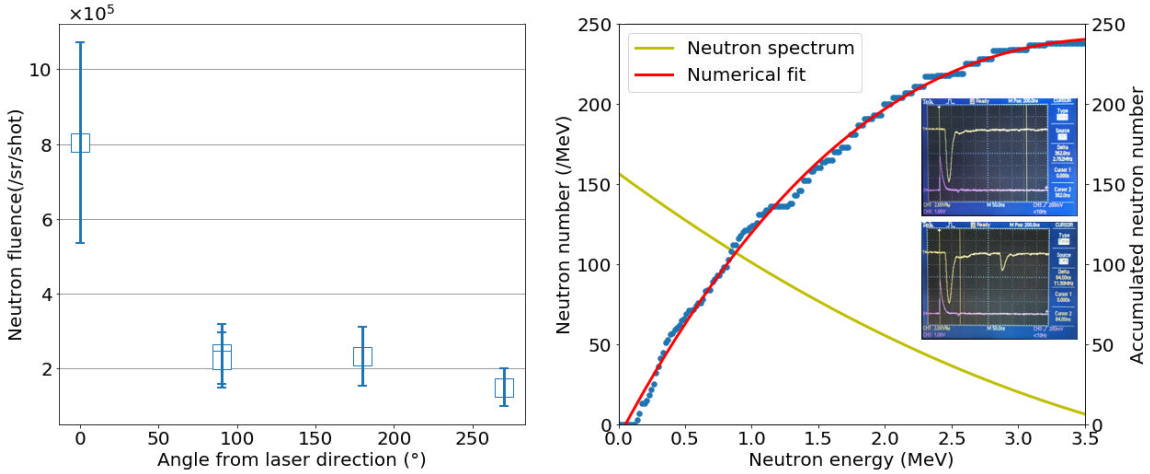

Figure 4.4: Left: neutron fluence angular distribution; Right: neutron energy distribution, averaged over 200 shots. The inset pictures are oscilloscope waveform of background γ-ray and neutron signal.

4.5 GEANT4 Simulation

To better understand the physics processes and optimize the neutron yield for future experiments, GEANT4 simulations were carried out using the measured electron energy distribution from the experiment. The configuration of the simulation consists of an aluminum target chamber, a 26.6 mm tungsten converter and two detector rings centered at the converter, one inside the chamber one outside the chamber. The detector rings were used to study the angular distribution of escaping electrons, γ-rays and neutrons. The detection thresholds were set to be 5 MeV for both electrons and γ-rays. For tungsten, the photoneutron cross-section falls to zero when photon energy is less than 5 MeV. The electron beam, sampled with Gaussian energy distribution centered at 37 MeV with σ=13 MeV, was launched towards the converter from the center of the chamber. The angular distribution of electrons was also set to have a Gaussian profile of 30mrad FWHM to match the property of measured electron beam. This simulation was run with 10^8 particles,

corresponding to 16 pC electron bunches, about 20% of the electrons generated in each experimental shot.

Figure 4.5 shows the reaction region for each physics process in the simulation. All color images are plotted on log scales and normalized so that the highest values are a thousand times bigger than the lowest one. Image (a) is the projection of electron energy deposition on the converter. It reveals that the converter is thick enough to stop most of the electrons from penetrating. Image (b) is the projection of γ-ray production due to Bremsstrahlung radiation. The production of γ-ray peaks at the front surface then decreases with increasing depth and forms a shape like a candle flame, similar to the electron energy deposition. The radiation lengths for electrons and photons do not overlap because the production of high energy γ-rays occurs predominantly in the first 5mm of the converter. This is in agreement with the fact that Bremsstrahlung radiation dominates above 20 MeV and its cross-section decreases as electron energy decreases, while energy loss due to collisions remains nearly constant. As electrons penetrate deeper, their energy decreases and more energy goes to ionization rather than γ-ray production. Because the detection threshold was set to be 5 MeV, the simulation also implies that the electrons lose its capability to create high energy γ-rays after 15mm, and therefore do not contribute to generating neutrons. Image c) is the projection of the total γ-ray scattering, including pair production, Compton scattering, and photo-nuclear activation. The "cut off" on the projection contour implies a "leakage" of γ-rays. Compared with electrons, γ-ray leakage is much more severe, which we believe is the main reason of the exaggerated neutron signal collected at the front direction. Comparing (b) and (c) shows that while most γ-rays were created at the front surface, γ-ray scattering happened much deeper in the converter. There is a delay between γ-ray production and γ-ray scattering which is approximately the mean

free path of a γ-ray in tungsten, suggesting an efficient way to create neutron sources and collimated γ-ray sources at the same facility simply by changing the thickness of converter.

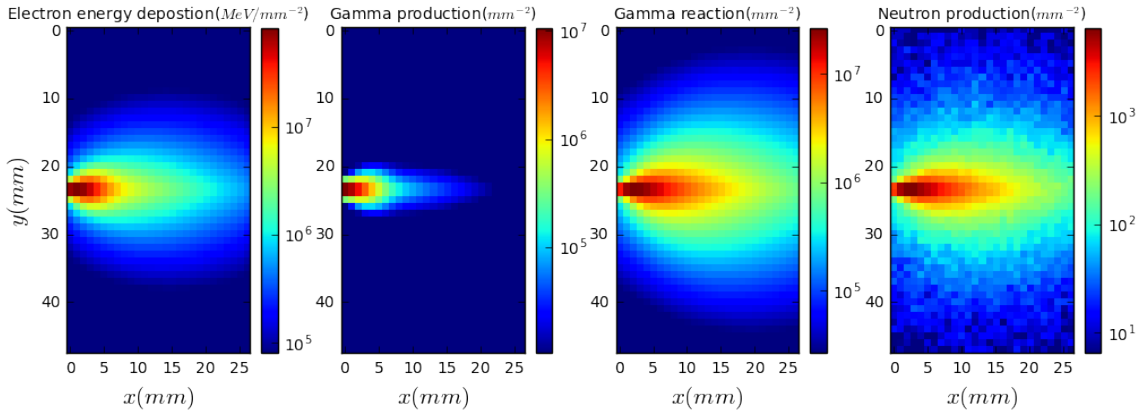

Figure 4.5: Projection plot of reaction inside the converter. Number was integrated along hidden axis and then normalize with highest value are 1000 times of lowest value. (a) Electron energy deposition indicate how much energy was deposit in certain location. (b) Projection plot of γ-ray (> 5 MeV) production via bremsstrahlung radiation, in unit of number of γ-ray produced per mm^2 (c) γ-ray (> 5 MeV) total scattering, including pair production, Compton scattering and photo-nuclear activation, in unit of number of reaction per mm^2 (d) Neutron produced via photo-nuclear reaction, in unit of number of neutron per mm^2.

Figure 4.6 shows the angular fluence distribution of the escaping electrons, γ-rays, and neutrons inside and outside the chamber. The 0 direction is the electron forward direction. The red line corresponds to the data collected at the detectors inside the chamber, the blue line represents the data acquired outside the chamber. As shown in the figure, both the escaping electrons and γ-rays go forward with a small divergence. Some electrons were scattered backward at the front surface and have a surface fluence following cosine law. Most electrons escaped from the converter were absorbed by the chamber wall. The electrons detected by the outer detectors were created by Compton scattering and pair production induced by escaping γ-rays, which had a fluence two magnitudes greater than

that of electrons. The neutrons, however, showed a nearly isotropic distribution, inside and outside the chamber, indicating that not many neutrons were created at the chamber wall. For this reason, we suspect that the bubble detector at 0 degree was affected by high energy electrons. Even though bubble detectors were claimed to be insensitive to γ-rays, they were not tested for their sensitivities to high energy electrons. Future experiments should be conducted to calibrate the response of bubble detector to high energy electrons. The isotropic neutron fluence detected in other directions also supports this interpretation, as the escaping electrons were very collimated, bubble detectors in other direction were not affected by these electrons. The average neutron fluence inside the chamber was found to be $4\times10^4 n/sr$, which is also about 20% of the neutrons we detected. The electron to neutron conversion efficiency is about 1/2500. Both agree very well with the experimental data.

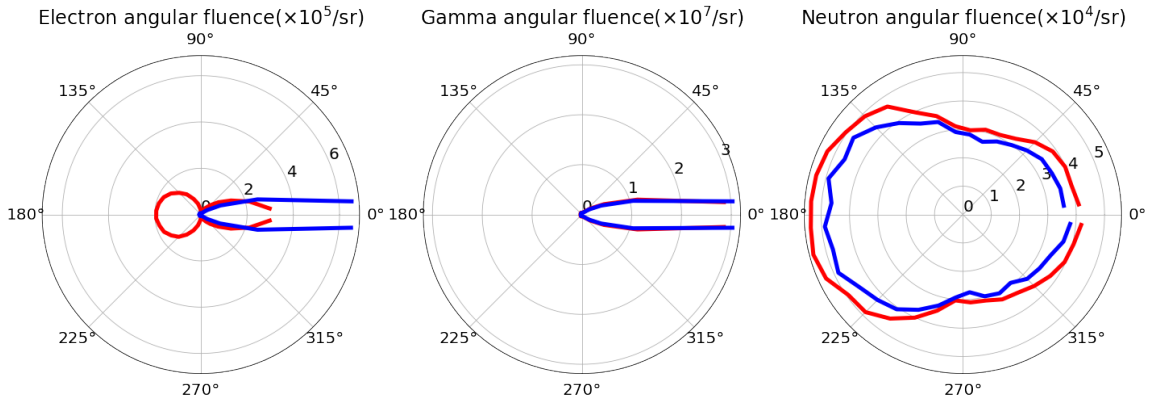

Figure 4.6: Left: electron angular fluence (> 5 MeV); Middle: γ-ray angular fluence. (> 5 MeV); Right: neutron angular fluence. The red line represents the fluence detector inside the chamber, the blue line represents the fluence detector outside the chamber.

Chapter 5: Summary and Conclusion

In conclusion, a neutron source with $> 2\times10^6$ neutrons per shot was created by using LWFA on a TW class laser. In this experiment, gas content and density were varied, the converter was designed to reach an optimum performance. The laser power is 15 times that of the critical power. The LWFA was found to be running at nonlinear broken wave regime and the laser pulse length is 2 times the plasma wave length. A PIC simulation was conducted to understand the dynamic of the interaction. The electron spectrum from the simulation was found qualitatively agree with the experimentally measured electron spectrum. The energy efficiency from laser to high energy electrons (>10MeV) is about 0.6%. The conversion efficiency from laser energy to neutron is greater than 4×10^6 neutrons/J, higher than most previous results on lasers of same class (Belyaev et al., 2006; Disdier, Garçonnet, Malka, & Miquel, 1999; Ditmire et al., 1999; Ellison & Fuchs, 2010; Leemans et al., 2001; Petrov et al., 2012; Reed et al., 2007).

In this experiment, the neutron pulse had a very short temporal structure of ~300 ps, which is estimated by the time that neutron bunches with median energy travel through the reaction region. The peak neutron emission rate was estimated to be $6.7\times10^{16}/s$. The number conversion efficiency from electrons to neutrons is about 1/2500, a number further confirmed by the GEANT4 simulation. The efficiency can be further improved by optimizing the converter profile in the aid of computer simulation. With upcoming high repetition kHz lasers, the neutron average flux can be improved as well, making this neutron source a prominent candidate for small applications such as neutron holography (Sarenac et al., 2016) and neutron resonance spectroscopy (Higginson et al., 2010).

Compared to ion driven neutron source, this technique has a much lower energy conversion efficiency mainly because most of the electron energy was lost due to pair production and subsequent electromagnetic shower, where energy eventually become thermal energy. The particle conversion efficiency from 37 MeV proton to neutron was roughly 1/2, which is a thousand times bigger than electron driven neutron source. However, this technique has an advantage of producing very short neutron pulse near the samples. Since all the high energy electrons travel at speed close to the speed of light, the dispersion of the electron bunch during traveling is much smaller than ion bunches. By directly creating neutron flux near the sample, the actual neutron pulse duration can be less than 1 ns, which is shorter than any of the conventional neutron sources currently available (Chou, 2004).

It should be understood that this experiment is only a small step in a series of experiments that may or may not lead to the compact and portable high flux neutron sources. It did not produce the highest neutron flux. However, it provides valuable knowledge about how things work in this condition, which can potentially contribute to finding a better solution.

Appendix

This experiment was conducted in the UT3 laser (University of Texas Two-Color Terawatt Laser) system at the University of Texas at Austin. The UT3 laser is a commercial system (Alpha 10/XS) from Thales Lasers. It is a TW class, 30~40 fs, 800 nm high contrast Ti:Sapphire laser, which can operate at 10-Hz. The schematic setup of this laser was illustrated below in Figure A.1 for interested readers.

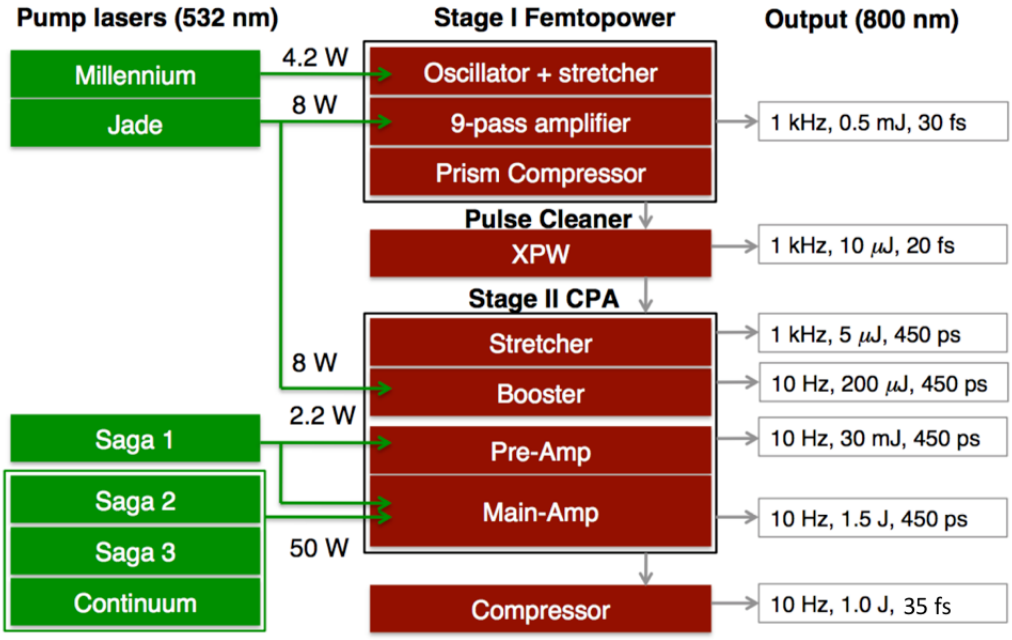

Figure A.1: The schematic setup and specification of UT3 laser system. Image credit: Hai-En Tsa

References

Barth, R. F., Coderre, J. A., Vicente, M. G. H., & Blue, T. E. (2005). Boron Neutron Capture Therapy of Cancer: Current Status and Future Prospects. *Clinical Cancer Research*, *11*(11), 3987–4002. https://doi.org/10.1158/1078-0432.CCR-05-0035

Belyaev, V. S., Vinogradov, V. I., Matafonov, A. P., Krainov, V. P., Lisitsa, V. S., Faenov, A. Y., … Kozlov, O. B. (2006). Neutron production in picosecond laser-generated plasma on a be target. *Physics of Atomic Nuclei*, *69*(6), 919–923. https://doi.org/10.1134/S1063778806060019

Bilheux, H. Z., McGreevy, R., & Anderson, I. S. (Eds.). (2009). *Neutron Imaging and Applications*. Boston, MA: Springer US. https://doi.org/10.1007/978-0-387-78693-3

Caldwell, R. L., & Mills, W. R. (1959). Activation analysis in petroleum exploration research. *Nuclear Instruments and Methods*, *5*(5), 312–322. https://doi.org/10.1016/0029-554X(59)90157-0

Chou, W. (2004). Spallation neutron source and other high internsity proton sources. *Accelerator Physics, Technology, and Applications: Selected Lectures of OCPA International Accelerator School 2002, Singapore*, 231.

Chubar, O., Elleaume, P., & Chavanne, J. (1998). A three-dimensional magnetostatics computer code for insertion devices. *Journal of Synchrotron Radiation*, *5*(3), 481–484. https://doi.org/10.1107/S0909049597013502

Copley, J. R. (2001). The fundamentals of neutron powder diffraction. *Special Publication (NIST SP)-*.

Dangendorf, V., Bar, D., Bromberger, B., Feldman, G., Goldberg, M. B., Lauck, R., … Weierganz, M. (2009). Multi-Frame Energy-Selective Imaging System for Fast-Neutron Radiography. *IEEE Transactions on Nuclear Science*, *56*(3), 1135–1140. https://doi.org/10.1109/TNS.2009.2014950

Disdier, L., Garçonnet, J.-P., Malka, G., & Miquel, J.-L. (1999). Fast Neutron Emission from a High-Energy Ion Beam Produced by a High-Intensity Subpicosecond Laser Pulse. *Physical Review Letters*, *82*(7), 1454–1457. https://doi.org/10.1103/PhysRevLett.82.1454

Ditmire, T., Zweiback, J., Yanovsky, V. P., Cowan, T. E., Hays, G., & Wharton, K. B. (1999). Nuclear fusion from explosions of femtosecond laser-heated deuterium clusters. *Nature*, *398*(6727), 489–492.

Ellison, C. L., & Fuchs, J. (2010). Optimizing laser-accelerated ion beams for a collimated neutron source. *Physics of Plasmas*, *17*(11), 113105. https://doi.org/10.1063/1.3497011

Esarey, E., Schroeder, C. B., & Leemans, W. P. (2009). Physics of laser-driven plasma-based electron accelerators. *Reviews of Modern Physics*, *81*(3), 1229–1285. https://doi.org/10.1103/RevModPhys.81.1229

Freiburghaus, C., Rosswog, S., & Thielemann, F.-K. (1999). r-Process in Neutron Star Mergers. *The Astrophysical Journal Letters*, *525*(2), L121. https://doi.org/10.1086/312343

Gupta, D. N., & Suk, H. (2007). Energetic electron beam generation by laser-plasma interaction and its application for neutron production. *Journal of Applied Physics*, *101*(11), 114908. https://doi.org/10.1063/1.2738377

Hegelich, B. M., Pomerantz, I., Yin, L., Wu, H. C., Jung, D., Albright, B. J., … Fernandez, J. C. (2013). Laser-driven ion acceleration from relativistically transparent nanotargets. *New Journal of Physics*, *15*(8), 085015. https://doi.org/10.1088/1367-2630/15/8/085015

Higginson, D. P., McNaney, J. M., Swift, D. C., Bartal, T., Hey, D. S., Kodama, R., … Beg, F. N. (2010). Laser generated neutron source for neutron resonance spectroscopy. *Physics of Plasmas*, *17*(10), 100701. https://doi.org/10.1063/1.3484218

Ing, H. (2001). Neutron measurements using bubble detectors — terrestrial and space. *Radiation Measurements*, *33*(3), 275–286. https://doi.org/10.1016/S1350-4487(00)00154-2

Jung, D., Falk, K., Guler, N., Deppert, O., Devlin, M., Favalli, A., … Roth, M. (2013). Characterization of a novel, short pulse laser-driven neutron source. *Physics of Plasmas*, *20*(5), 056706. https://doi.org/10.1063/1.4804640

Lancaster, K. L., Karsch, S., Habara, H., Beg, F. N., Clark, E. L., Freeman, R., … Zepf, M. (2004). Characterization of 7Li(p,n)7Be neutron yields from laser produced ion beams for fast neutron radiography. *Physics of Plasmas*, *11*(7), 3404–3408. https://doi.org/10.1063/1.1756911

Leemans, W. P., Rodgers, D., Catravas, P. E., Geddes, C. G. R., Fubiani, G., Esarey, E., … Smith, A. (2001). Gamma-neutron activation experiments using laser wakefield accelerators. *Physics of Plasmas*, *8*(5), 2510–2516. https://doi.org/10.1063/1.1352617

Macchi, A., Borghesi, M., & Passoni, M. (2013). Ion acceleration by superintense laser-plasma interaction. *Reviews of Modern Physics*, *85*(2), 751–793. https://doi.org/10.1103/RevModPhys.85.751

Petrov, G. M., Higginson, D. P., Davis, J., Petrova, T. B., McNaney, J. M., McGuffey, C., … Beg, F. N. (2012). Generation of high-energy (>15 MeV) neutrons using short pulse high intensity lasers. *Physics of Plasmas*, *19*(9), 093106. https://doi.org/10.1063/1.4751460

Pomerantz, I., McCary, E., Meadows, A. R., Arefiev, A., Bernstein, A. C., Chester, C., … Hegelich, B. M. (2014). Ultrashort Pulsed Neutron Source. *Physical Review Letters*, *113*(18). https://doi.org/10.1103/PhysRevLett.113.184801

Pukhov, A., & Meyer-ter-Vehn, J. (2002). Laser wake field acceleration: the highly non-linear broken-wave regime. *Applied Physics B: Lasers and Optics*, *74*(4–5), 355–361. https://doi.org/10.1007/s003400200795

Reed, S. A., Chvykov, V., Kalintchenko, G., Matsuoka, T., Yanovsky, V., Vane, C. R., … Maksimchuk, A. (2007). Efficient initiation of photonuclear reactions using quasimonoenergetic electron beams from laser wakefield acceleration. *Journal of Applied Physics*, *102*(7), 073103. https://doi.org/10.1063/1.2787159

Roth, M., Jung, D., Falk, K., Guler, N., Deppert, O., Devlin, M., … Wurden, G. A. (2013). Bright Laser-Driven Neutron Source Based on the Relativistic Transparency of Solids. *Physical Review Letters*, *110*(4). https://doi.org/10.1103/PhysRevLett.110.044802

Roth, M., Jung, D., Falk, K., Guler, N., Deppert, O., Devlin, M., … Wurden, G. A. (2016). A bright neutron source driven by relativistic transparency of solids. *Journal of Physics: Conference Series*, *688*, 012094. https://doi.org/10.1088/1742-6596/688/1/012094

Sarenac, D., Huber, M. G., Heacock, B., Arif, M., Clark, C. W., Cory, D. G., … Pushin, D. A. (2016). Holography with a neutron interferometer. *Optics Express*, *24*(20), 22528. https://doi.org/10.1364/OE.24.022528

Tajima, T., & Dawson, J. M. (1979). Laser Electron Accelerator. *Physical Review Letters*, *43*(4), 267–270. https://doi.org/10.1103/PhysRevLett.43.267

Taylor, A., Dunne, M., Bennington, S., Ansell, S., Gardner, I., Norreys, P., … Nelmes, R. (2007). A Route to the Brightest Possible Neutron Source? *Science*, *315*(5815), 1092–1095. https://doi.org/10.1126/science.1127185

Tsai, H.-E., Wang, X., Shaw, J. M., Li, Z., Arefiev, A. V., Zhang, X., … Downer, M. C. (2015). Compact tunable Compton x-ray source from laser-plasma accelerator and plasma mirror. *Physics of Plasmas*, *22*(2), 023106. https://doi.org/10.1063/1.4907655

Wang, X., Zgadzaj, R., Fazel, N., Li, Z., Yi, S. A., Zhang, X., … Downer, M. C. (2013). Quasi-monoenergetic laser-plasma acceleration of electrons to 2 GeV. *Nature Communications*, *4*. https://doi.org/10.1038/ncomms2988

Wilks, S. C., Langdon, A. B., Cowan, T. E., Roth, M., Singh, M., Hatchett, S., … Snavely, R. A. (2001). Energetic proton generation in ultra-intense laser–solid interactions. *Physics of Plasmas*, *8*(2), 542–549. https://doi.org/10.1063/1.1333697

Willingale, L., Petrov, G. M., Maksimchuk, A., Davis, J., Freeman, R. R., Joglekar, A. S., … Krushelnick, K. (2011). Comparison of bulk and pitcher-catcher targets for laser-driven neutron production. *Physics of Plasmas*, *18*(8), 083106. https://doi.org/10.1063/1.3624769

Wu, Y. C., Zhu, B., Dong, K. G., Yan, Y. H., & Gu, Y. Q. (2012). Note: Absolute calibration of two DRZ phosphor screens using ultrashort electron bunch. *Review of Scientific Instruments*, *83*(2), 026101. https://doi.org/10.1063/1.3681442